MATHEMATICAL MODELING AND NUMERICAL SIMULATION OF TELEPHONE CORD BUCKLES OF ELASTIC FILMS

SHAN WANG AND ZHIPING LI †

LMAM & SCHOOL OF MATHEMATICAL SCIENCES,
PEKING UNIVERSITY, BEIJING 100871, P.R.CHINA

ABSTRACT. An annular sector model for the telephone cord buckles of elastic thin films on rigid substrates is established, in which the von Kárman plate equations in polar coordinates are used for the elastic thin film and a discrete version of the Griffith criterion is applied to determine the shape and scale parameters. A numerical algorithm combining the Newmark-β scheme and the Chebyshev collocation method is designed to numerically solve the problem in a quasi-dynamic process. Numerical results are presented to show that the numerical method works well and the model agrees well with physical observations, especially successfully simulated for the first time the telephone cord buckles with two humps along the ridge of each section of a buckle.

Keywords: elastic film, telephone cord buckles, von Kárman plate equations, Griffith criterion, Chebyshev collocation method.

1. INTRODUCTION

Thin film materials are wildly used in many fields, such as thermal barrier coatings [1], microelectromechanical systems [2], magnetic recording media [3], etc. However, compressed residual stresses are generally inevitably introduced on the elastic thin films in manufacturing processes, which can lead to undesirable delamination in the interface of the thin film and the substrate. The delaminated thin film will buckle to release the stored elastic energy and will

2000 *Mathematics Subject Classification.* 65M70,74B20,74G15,74G60,74K35,74R99,74S25.
Key words and phrases. elastic film, von Karman plate, delamination, buckling, Chebyshev collocation method.

† Corresponding author: Zhiping Li, email address: lizp@math.pku.edu.cn
The research was supported by the Major State Basic Research Projects (2005CB321701), NSFC projects 10871011 and RFDP of China.

eventually form certain wrinkling patterns. It is of great interest to reveal the underline mechanisms of the buckling process, and studying the morphology of the buckles is a part of the effort.

In the study of the delamination and buckling phenomenon, the thin film is considered to be a thin elastic plate, thus the von Kárman plate equations are used as the governing equations, and the delamination is considered to be the result of growing fractures when the film is peeled off from the substrate. According to the fracture mechanics, the energy release rate G^* and the phase angle ψ at the fracture front are considered to be the characteristic quantities in the thin film delamination. The Griffith criterion of the form $G^* \geq \Gamma^*$, where Γ^* is the interface toughness, is often used to determine whether a crack front will propagate, and the phase angle ψ describes the fracture mode-mixity [4–6].

Various kinds of buckling patterns are reported to be observed in physical experiments and real world applications, and the circular buckles [7], straight-sided buckles [8, 9] and telephone-cord buckles [7, 10–15] are believed to be the most commonly observed patterns. The circular buckles are well investigated, and the detailed analysis can be found in [16]. The straight-sided buckles have also well studied by many researchers in the last decades [16–21].

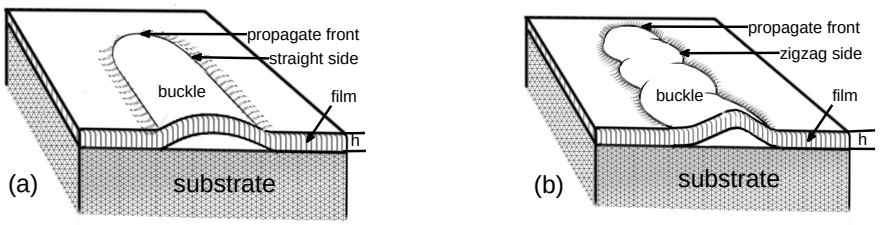

FIGURE 1: The geometries of a straight-sided (a) and telephone cord buckles (b).

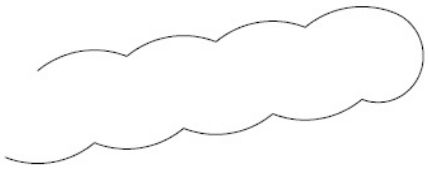

FIGURE 2: Gioia and Ortiz model

Similar to a straight-sided buckle, which has two straight parallel crack lines on each side of the buckle and curved propagation fronts as illustrated schematically in Figure 1, a telephone cord buckle also propagates with curved fronts, but leaves behind long telephone cord like zigzagged "parallel" crack lines. Although, compared with other types of buckles' morphology, the telephone cord buckles are the most easily reproduced buckle pattern in physical experiments, their mathematical modeling is not as well established. In 1997, applying the Griffith criterion and assuming that the energy release rate is identical everywhere on the fracture front, Gioia and Ortiz established a model in which the zigzagged edges of the telephone cord are approximated by many connected congruent circular arcs, and the propagation fronts are also approximated by circular arcs but in a different size (Figure 2). The model describes the shape of the edges successfully and fits experimental results well [22], however, it cannot determine the widths of the telephone cord buckles. In 2002, Moon et al. established a pinned circle model, in which the delamination area is characterized by a sequence of connected sectors (Figure 3) and on each sector the deformation of the buckle is assumed to be rotationally symmetric with respect to the pinned center [15]. The model well describes both the shape of the edges and the width of the telephone cord. However, because of the rotationally symmetric assumption, the connecting point (O in Figure 3 (a)) is a singular point for the energy release rate and the global deformation is discontinuous across the connection lines between the sectors ($\overline{OB}$ in Figure 3 (a)).

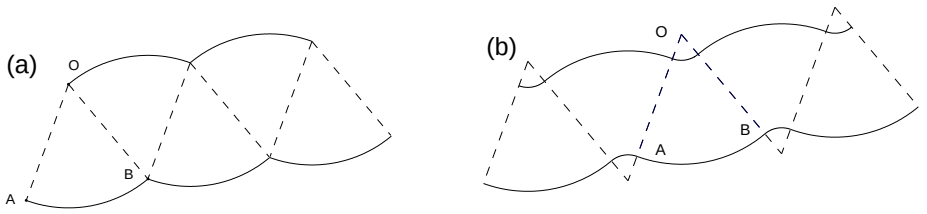

FIGURE 3: The pinned circle model (a): O is the center of the sector AOB . The annular sector model (b): delamination area is divided into congruent annular sectors. The dashed lines are the connection lines between adjacent sectors. O is the center of the sector AOB

In the present paper, stimulated by the physical observations, an annular sector model is developed. In this model, the zigzagged part of the buckle is assumed to be composed of a sequence of congruent annular sectors (Figure 3 (b)), and both the deformation and its derivatives are assumed to be globally

continuous. The shape and size of the buckle are characterized by three parameters, i.e. the inner and outer radii, and the central angle of the annular sector, which will be determined by a discrete version of the Griffith criterion. To numerically solve the derived system of equations, which is highly nonlinear with multiple solutions and bifurcations, a quasi-dynamic process is adopted and a numerical algorithm combining the Newmark-β scheme and the Chebyshev collocation method is developed. It turns out that the model allows us to capture the characteristics of the telephone cord buckles more efficiently. In fact, our numerical experiments show that the model agrees well with the physical observations. Especially, we successfully simulated the telephone cord buckles with two humps along the ridge of each section of a buckle (see Figure 6 and compare it with figure 2 in [13]), to our knowledge this is the first numerical result of the kind.

The rest of the paper is organized as follows. The annular sector model of the telephone cord buckles is established in Section 2. In Section 3, a numerical method combining the Newmark-β scheme and the Chebyshev collocation method is developed for the highly nonlinear coupled von Kárman plate equations. Numerical experiments and results are presented and discussed in Section 4. In Section 5, the numerical results are further analyzed and compared with cetain well known physical experiments. The paper ends with a brief summary in Section 6.

2. The annular sector model

2.1. **The morphology assumptions and parameters.** Numerous physical experiments reveal that, the total length of a telephone cord buckle is usually much bigger than its width ([15], Fig. 6), and away from the propagation fronts, the zigzagged part of a telephone cord buckle essentially consists of a number of smoothly connected nearly identical sections, each of these sections looks like an annular sector with a relatively much smaller inner radius (see images in [7, 12, 22, 23]), in addition, the best part of the two zigzagged edges of a telephone cord buckle are roughly "parallel" to each other. Motivated by these observations, we establish the annular sector model of the telephone cord buckles by making the following morphology assumptions:

1: the sections are congruent annular sectors, and the relative deformation on each section is also identical;

2: the deformation on each annular sector is symmetric with respect to its geometric symmetry axis, i.e. the line l in Figure 4;

3: the buckling deformation is smooth, and thus the deformation and its derivatives are continuous across the connected annular sectors.

It follows from the morphology assumption 1 that, the shape and the width scale of a telephone cord buckle can be completely determined by three parameters. For simplicity, we choose the outer radius R of the annular sector as the scale parameter, the half central angle θ_0 (see Figure 4) and the normalized inner radius r_0, i.e. the ratio of the inner radius against the outer radius, of the annular sector as the shape parameters.

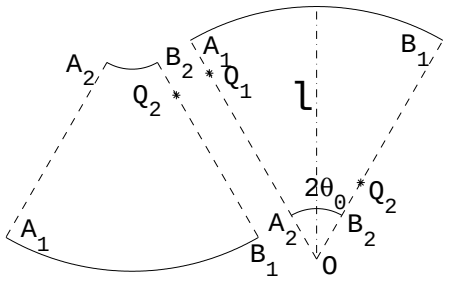

FIGURE 4: A typical section: O is the center of the sector, $\overline{OA_1}$ and $\overline{OA_2}$ are the outer and inner radii with $|\overline{OA_1}| = R$ and $|\overline{OA_2}|/|\overline{OA_1}| = r_0$, $\angle A_1OB_1 = 2\theta_0$ is the central angle. Q_1 and Q_2 with $|\overline{Q_1A_1}| = |\overline{Q_2B_2}|$ are the reciprocally corresponding connection points across which the deformation is smooth.

2.2. **Governing equations and boundary conditions.** According to the morphology assumption 1, the governing equations of the equilibrium state of the buckle can be reduced to the von Kárman plate equations defined on an annular sector Ω^*. Naturally, it is convenient to express the equations in the polar coordinate system (r^*, θ^*) with the annular sector's center O as the polar origin and the sector's geometric symmetry line l as the polar axis (Figure 4). For simplicity, we assume that the initial residual stress is equi-biaxial compressive, in Cartesian coordinates this is expressed as $-\sigma_{xx} = -\sigma_{yy} = \sigma_0^* > 0$, $\sigma_{xy} = 0$.

For the convenience of numerical experiments, we will write the von Kárman plate equations in terms of dimensionless variables. Let R be the outer radius of the annular sector, and let $h^* \ll R$ be the thickness of the film. Let w^*, u^*, and v^* be the out-of-plane, radial in-plane and tangent in-plane displacements of the buckle respectively. Denote $(r,\,\theta)$, σ_0, h, w, u and v the corresponding normalized dimensionless variables defined by

$$r = \frac{r^*}{R},\ \theta = \theta^*,\ \sigma_0 = 4\pi^2\frac{\sigma_0^*}{\sigma_c^*},\ h = \frac{h^*}{R},\ w = \frac{w^*}{h^*},\ u = \frac{Ru^*}{(h^*)^2},\ v = \frac{Rv^*}{(h^*)^2}, \quad (2.1)$$

where $\sigma_c^* = \bar{E}(\pi h^*)^2/(3R^2)$ is the critical bifurcation stress for straight-sided buckles of width R. In terms of the normalized displacements w, u and v, which are functions of $(r,\,\theta)$ defined on the normalized annular sector region $\Omega = \{(r,\,\theta)|r_0 < r < 1,\ -\theta_0 < \theta < \theta_0\}$, the load free von Kárman plate equations are expressed as

$$\begin{cases} \triangle^2 w - \sigma_0 \triangle w = NLT_W(w,u,v), \\ LT_U(u,v) + NLT_U(w) = 0, \qquad\qquad (r,\,\theta) \in \Omega, \\ LT_V(u,v) + NLT_V(w) = 0, \end{cases} \quad (2.2)$$

where $\triangle = \dfrac{\partial^2}{\partial r^2} + \dfrac{1}{r}\dfrac{\partial}{\partial r} + \dfrac{1}{r^2}\dfrac{\partial^2}{\partial\theta^2}$, $\triangle^2 = \left(\dfrac{\partial^2}{\partial r^2} + \dfrac{1}{r}\dfrac{\partial}{\partial r} + \dfrac{1}{r^2}\dfrac{\partial^2}{\partial\theta^2}\right)^2$, and the linear terms and non-linear terms are given by

$$\begin{aligned} NLT_W = \ & 12[(A+\nu B)w_{,rr} + \frac{1}{r}(\frac{1}{r}w_{,\theta\theta} + w_{,r})(B+\nu A) \\ & + \frac{1}{r}(1-\nu)(w_{,r\theta} - \frac{1}{r}w_{,\theta})(v_{,r} + \frac{1}{r}(u_{,\theta} - v + w_{,r}\,w_{,\theta}))], \end{aligned}$$

with $A = \dfrac{1}{2}w_{,r}^2 + u_{,r}$ and $B = \dfrac{1}{r}((u + v_{,\theta}) + \dfrac{1}{2r}w_{,\theta}^2)$, and

$$\begin{aligned} LT_U &= 2(-\frac{1}{r^2}u + \frac{1}{r}u_{,r} + u_{,rr}) + (1-\nu)\frac{1}{r^2}u_{,\theta\theta} + (1+\nu)\frac{1}{r}v_{,r\theta} + (3-\nu)\frac{1}{r^2}v_{,\theta}\,, \\ LT_V &= (1-\nu)(-\frac{1}{r^2}v + \frac{1}{r}v_{,r} + v_{,rr}) + 2\frac{1}{r^2}v_{,\theta\theta} + (1+\nu)\frac{1}{r}u_{,r\theta} + (3-\nu)\frac{1}{r^2}u_{,\theta}\,, \\ NLT_U &= 2w_{,r}\,w_{,rr} + \frac{1}{r}(1-\nu)w_{,r}\,(w_{,r} + \frac{1}{r}w_{,\theta\theta}) + \frac{1}{r^2}(1+\nu)w_{,\theta}\,(w_{,r\theta} - \frac{1}{r}w_{,\theta}), \\ NLT_V &= 2w_{,\theta}\,w_{,\theta\theta} + \frac{1}{r}(1-\nu)w_{,\theta}\,(w_{,rr} + \frac{1}{r}w_{,r}) + \frac{1}{r}(1+\nu)w_{,r}\,w_{,r\theta}\,. \end{aligned}$$

Since the solution $(w(r,\theta), u(r,\theta), v(r,\theta))$ of the equations (2.2) depends on the domain parameters (r_0, θ_0), it is also denoted as $(w(r,\theta;r_0,\theta_0),\ u(r,\theta;r_0,\theta_0),\ v(r,\theta;r_0,\theta_0))$, when we want to emphasis the relation.

Next, we consider the boundary conditions. According to the morphology assumption 3, i.e. the smoothness of the deformation, the clamped boundary conditions are imposed on the arced edges of the annular sector (solid lines in Figure 3 (b) and Figure 4), and the continuity conditions for the deformation and its certain derivatives are imposed on the reciprocally corresponding connection points on the two radial edges, i.e. if $Q_1 \in \overline{A_1A_2}$ and $Q_2 \in \overline{B_1B_2}$ satisfy $|\overline{A_1Q_1}| = |\overline{B_2Q_2}|$, then their deformation should be smoothly connected. More precisely, we have the clamped boundary conditions

$$\begin{cases} w(r_0,\theta)=0,\ w_{,r}(r_0,\theta)=0,\ u(r_0,\theta)=0,\ v(r_0,\theta)=0, \\ w(1,\theta)=0,\quad w_{,r}(1,\theta)=0,\quad u(1,\theta)=0,\quad v(1,\theta)=0, \end{cases} \tag{2.3}$$

and the reciprocally periodic connection boundary conditions

$$\begin{cases} \dfrac{1}{r^k}\dfrac{\partial^k w}{\partial\theta^k}\Big|_{(r,-\theta_0)} = \dfrac{1}{(1+r_0-r)^k}\dfrac{\partial^k w}{\partial\theta^k}\Big|_{(1+r_0-r,\,\theta_0)}, \qquad k=0,1,2,3, \\ u(r,-\theta_0) = -u(1+r_0-r,\theta_0),\ \dfrac{u_{,\theta}(r,-\theta_0)}{r} = -\dfrac{u_{,\theta}(1+r_0-r,\theta_0)}{1+r_0-r}, \\ v(r,-\theta_0) = v(1+r_0-r,\theta_0),\quad \dfrac{v_{,\theta}(r,-\theta_0)}{r} = \dfrac{v_{,\theta}(1+r_0-r,\theta_0)}{1+r_0-r}. \end{cases} \tag{2.4}$$

2.3. **Determination of the shape and scale parameters.** Let E and ν be the Young's modulus and Poisson's ratio of the elastic thin film respectively, and denote $\bar{E} = E/(1-\nu^2)$. Let $G_0^* = h^*\sigma_0^{*2}/(2\bar{E})$, which is known to be the strain energy per unit area when the film is released in plane strain [16]. Then, the energy release rate G^*, the normalized energy release rate G and the phase angle ψ [16, 20, 24, 25], which are defined on the fracture fronts where $r = r_0$ or 1, are given in the polar coordinate system as

$$G(r,\theta;r_0,\theta_0) = \left(w_{,rr} + \frac{\nu}{r^2}w_{,r\theta}\right)^2 + 12u_{,r}^2, \tag{2.5}$$

$$G^*(r,\theta;R,r_0,\theta_0) = \frac{3G_0^*}{4\pi^4\sigma_0^2}G(r,\theta;r_0,\theta_0) = \frac{\bar{E}h^{*5}}{384\pi^4R^4}G(r,\theta;r_0,\theta_0), \tag{2.6}$$

$$\psi(r,\theta;r_0,\theta_0)=\arctan\left(\frac{(w_{,rr}+\frac{\nu}{r^2}w_{,r\theta})\cos\omega+\sqrt{12}u_{,r}\sin\omega}{-(w_{,rr}+\frac{\nu}{r^2}w_{,r\theta})\sin\omega+\sqrt{12}u_{,r}\cos\omega}\right), \tag{2.7}$$

where $w_{,rr}=w_{,rr}(r,\theta;r_0,\theta_0)$, $w_{,r\theta}=w_{,r\theta}(r,\theta;r_0,\theta_0)$, and $u_{,r}=u_{,r}(r,\theta;r_0,\theta_0)$; and where ω is a function of Dundurs' parameter α [6] approximately given in the degree measure by $\omega(\alpha)=52.10+8.691\alpha+6.450\alpha^2+4.893\alpha^3$ [26]. For simplicity of notations, we often omit the shape parameters (r_0,θ_0) and denote $G(r,\theta;r_0,\theta_0)$ and $\psi(r,\theta;r_0,\theta_0)$ as $G(r,\theta)$ and $\psi(r,\theta)$ respectively.

For a given normalized initial residual stress σ_0, in applying the Griffith criterion principle to determine the shape parameters (r_0,θ_0) and the scale parameter R, instead of assuming the energy release rate G to be a constant along the fracture front, which can not possibly be satisfied in general since there are only two shape parameters to be determined, we require G to have the least variance along the zigzagged arcs and its mean value equals the normalized interface toughness $\Gamma(R)$, which relates to the original interface toughness Γ^* in the same way as G relates to G^*, i.e. $\Gamma(R)=\dfrac{384\pi^4R^4}{\bar{E}h^{*5}}\Gamma^*$.

In discrete form, the principle is realized in the following way. For fixed (r_0,θ_0), let $\alpha_j=j\theta_0/L$, $-L\le j\le L-1$, let $G(r,\theta)$ be the energy release rate obtained by substituting the numerical solution into the formula (2.5). Denote

$$\begin{aligned}\mathcal{G}_0&=(G(r_0,\alpha_{-L}),\ \cdots,\ G(r_0,\alpha_0),\ \cdots,\ G(r_0,\alpha_{L-1}))^T,\\ \mathcal{G}_1&=(G(1,\alpha_{-L}),\ \cdots,\ G(1,\alpha_0),\ \cdots,\ G(1,\alpha_{L-1}))^T.\end{aligned}$$

Define

$$m(r_0,\theta_0)=\frac{\mathrm{mean}(\mathcal{G}_0)+\mathrm{mean}(\mathcal{G}_1)}{2}, \tag{2.8}$$

$$S(r_0,\theta_0)=\frac{1}{4L}\sum_{j=-L}^{L-1}\left((G(r_0,\alpha_j)-m(r_0,\theta_0))^2+(G(1,\alpha_j)-m(r_0,\theta_0))^2\right), \tag{2.9}$$

where $\mathrm{mean}(\mathcal{G}_i)$ stands for the arithmetic means of $\mathcal{G}_i$. Obviously, $\mathrm{m}(r_0,\theta_0)$ and $\mathrm{S}(r_0,\theta_0)$ are the mean value and variance of the set $\{\mathcal{G}_0,\mathcal{G}_1\}$. With these notations, the principle is summarized as the shape and the scale criteria below:

Shape criterion: the shape parameters $(\hat{r}_0,\, \hat{\theta}_0)$ are so determined that they minimizes the variance $S(r_0, \theta_0)$, i.e.

$$(\hat{r}_0,\, \hat{\theta}_0) = \arg \min_{(r_0,\, \theta_0)} S(r_0,\, \theta_0). \tag{2.10}$$

Scale criterion: the scale parameter R is so determined that it solves

$$\Gamma(R) \triangleq \frac{384\pi^4 R^4}{\bar{E} h^{*5}} \Gamma^* = m(\hat{r}_0,\, \hat{\theta}_0). \tag{2.11}$$

3. Numerical scheme

3.1. **von Kárman dynamic system.** We adopt a dynamic approach to solve the static von Kárman equations (2.2). Noticing that the velocity and acceleration of the in-plane displacements are always very small around the static solutions, we restrict ourselves to the simplified von Kárman dynamic equations

$$\begin{cases} w_{,tt} + c w_{,t} + \triangle^2 w - \sigma_0 \triangle w - NLT_W(w, u, v) = 0, \\ LT_U(u, v) + NLT_U(w) = 0, \\ LT_V(u, v) + NLT_V(w) = 0, \end{cases} \tag{3.1}$$

where t and c are the dimensionless time and viscosity coefficient, which relate to the physical time t^* and viscosity coefficient c^* by

$$t = t^* \frac{h^*}{R^2} \sqrt{\frac{\bar{E}}{\rho}}, \qquad c = c^* \frac{R^2}{h^* \sqrt{\rho \bar{E}}}, \tag{3.2}$$

where ρ is the mass density of the thin film.

The system is completed by coupling the clamped boundary conditions (2.3) and the reciprocally periodic connection boundary conditions (2.4).

We start from small σ_0, when a buckle barely appears, and choose small smooth functions, such as $w_0 = \epsilon(1 - r)^2(r_0 - r)^2, u_0 = 0, v_0 = 0$ with small coefficient ϵ, as the initial value, then apply the continuation method in such a way that the numerical solution for the current σ_0 is taken as the initial value for the adjacent parameters $(r_0, \theta_0, \sigma_0)$ with a slightly increased σ_0. Noticing that, as a consequence of the morphology assumption 2, the solution to the von

Kárman equations (2.2) satisfies the symmetric relations

$$w(r,\theta) = w(r,-\theta), \quad u(r,\theta) = u(r,-\theta) \quad \text{and} \quad v(r,\theta) = -v(r,-\theta), \tag{3.3}$$

the initial values provided for the dynamic system should also satisfy (3.3).

3.2. **Temporal discretization.** To simplify the notations, we first rewrite the equations (3.1) in the following form

$$\begin{cases} w_{,tt} + cw_{,t} = F(w, \mathbf{U}), \\ \mathcal{L}(\mathbf{U}) = \mathbf{f}(w), \end{cases} \tag{3.4}$$

where $\mathbf{U} = (u,v)^T$, $F(w,\mathbf{U}) = -\triangle^2 w + \sigma_0 \triangle w + NLT_W(w,u,v)$, $\mathcal{L}(\mathbf{U}) = (LT_U(u,v), LT_V(u,v))^T$, $f(w) = -(NLT_U(w), NLT_V(w))^T$.

Follow the work of Yosibash et. al. [27], the application of the average acceleration variant of the Newmark-β scheme ([28] with Newmark parameters $\gamma = \frac{1}{2}$ and $\beta = \frac{1}{4}$) to the first equation of (3.4) leads to the following scheme

$$\begin{cases} \Big(\frac{4}{(\Delta t)^2} + \frac{2c}{\Delta t}\Big) w^{n+1} = F(w^{n+1}, \mathbf{U}^n) + \Big(\frac{4}{(\Delta t)^2} w^n + \frac{4}{\Delta t} w_{,t}^n + w_{,tt}^n\Big) \\ \qquad\qquad\qquad\qquad + c\Big(\frac{2}{\Delta t} w^n + w_{,t}^n\Big), \\ \mathcal{L}(\mathbf{U}^{n+1}) = \mathbf{f}(w^{n+1}). \end{cases} \tag{3.5}$$

We modify the scheme (3.5) by using the centered time differences to substitute the corresponding time derivatives appeared in the right hand side of (3.5), obtaining our semi-discrete implicit scheme

$$\Big(\frac{4}{(\Delta t)^2} + \frac{2c}{\Delta t}\Big) w^{n+1} = F(w^{n+1}, \mathbf{U}^n) + \Big(\frac{3}{(\Delta t)^2} + \frac{c}{2\Delta t}\Big) w^{n+1} + 2\Big(\frac{1}{(\Delta t)^2} + \frac{c}{\Delta t}\Big) w^n - \Big(\frac{1}{(\Delta t)^2} + \frac{c}{2\Delta t}\Big) w^{n-1}, \tag{3.6}$$

$$\mathcal{L}(\mathbf{U}^{n+1}) = \mathbf{f}(w^{n+1}). \tag{3.7}$$

We remark here that using $F(w^{n+1}, \mathbf{U}^n)$ instead of $F(w^{n+1}, \mathbf{U}^{n+1})$ as in [29] will definitely reduce tremendous amount of computing cost, though it may also lose some accuracy. However, remember that our aim is to obtain the solution of the static von Kárman equations, the stability and efficiency rather than the temporal accuracy is of more interest.

3.3. **Spatial discretization.** To fully discretize the system, we use the Chebyshev pseudo-spectral collocation method for the spatial discretization. Map the normalized annular sector domain $\Omega = \{(r,\theta)\big| r_0 \le r \le 1,\ -\theta_0 \le \theta \le \theta_0\}$ into the standard computational domain $\hat{\Omega} = \{(x,y)\big| -1 \le x \le 1,\ -1 \le y \le 1\}$ with

$$x = \frac{2r - 1 - r_0}{1 - r_0}, \quad y = \frac{\theta}{\theta_0}.$$

We rewrite the out-of-plane dimensionless displacement $w(x,y)$ in the form [27]:

$$w(x,y) = (x^2 - 1)q(x,y), \tag{3.8}$$

so that $q(x,y)$ satisfies the same set of boundary conditions as $u(x,y)$ and $v(x,y)$ on $x = \pm 1$ (see (2.3)), this makes it easier to choose a unified approach for the discretization and the choice of collocation points.

Let $T_i(x) = \cos\left(i\cos^{-1}(x)\right)$, $i = 0, 1, 2, \cdots$, be the Chebyshev polynomials of degree i. We discretize w^n, u^n and v^n into the following form:

$$w^n_{M,N}(x,y) = \sum_{i=0}^{M}\sum_{j=0}^{N+2}(x^2-1)\hat{q}^n_{ij}T_i(x)T_j(y), \tag{3.9}$$

$$u^n_{M,N}(x,y) = \sum_{i=0}^{M}\sum_{j=0}^{N}\hat{u}^n_{ij}T_i(x)T_j(y), \tag{3.10}$$

$$v^n_{M,N}(x,y) = \sum_{i=0}^{M}\sum_{j=0}^{N}\hat{v}^n_{ij}T_i(x)T_j(y). \tag{3.11}$$

Next, we consider the collocation points. Since $F(w^{n+1}, U^n)$ in equation (3.6) involves fourth derivatives of w^{n+1} in both x and y, and there are two boundary conditions for $q^{n+1}(x,y)$ at $x = \pm 1$ (see (2.3)) and four reciprocally periodic connection boundary conditions at $y \pm 1$ (see (2.4)), to have a consistent spatial discretization of the equation, we need

- **(i):** $M+1$ collocation points $\{x_i\}_{i=0}^{M}$ including $M-1$ distinct interior points satisfying $x_i = -x_{N-i}$ and 2 end points $x_0 = -1$, $x_N = 1$;
- **(ii):** $N+3$ collocation points $\{\tilde{y}_j\}_{j=0}^{N+2}$ including $N-1$ distinct interior points and 4 end points $\tilde{y}_0 = \tilde{y}_1 = -1$ and $\tilde{y}_{N+1} = \tilde{y}_{N+2} = 1$.

Similarly, for the equation (3.7), we need (i) and

(iii): $N+1$ collocation points $\{y_j\}_{j=0}^{N}$ including $N-1$ distinct interior points and 2 end points $y_0=-1$ and $y_N=1$.

It is easy to verify that the Chebyshev-Gauss-Lobatto collocation points for x and y, which are given as $x_i=\cos(i\pi/M)$, $i=0,1,2,\cdots,M$, and $y_j=\cos(j\pi/N)$, $j=0,1,2,\cdots,N$, meet the requirements (i) and (iii) respectively.

We follow the idea of constructing the Gauss-Lobatto type collocation points [30] to develop a set of collocation points with four-end-points. Let $\{P_k\}_{k=0}^{+\infty}$, with $P_n(y)=\dfrac{(n+3)T_{n+4}(y)-2T_{n+2}(y)-(n+1)T_n(y)}{(1-y^2)^2}$, $(n=0,1,2,\cdots)$, be the sequence of orthogonal polynomials on $[-1,1]$ with the weight function $\hat{W}(y)=(1-y^2)^{\frac{3}{2}}$. It can be shown that $P_k(y)$ has k distinct zero points $-1<\hat{y}_1^k<\hat{y}_2^k<\cdots<\hat{y}_k^k<1$, which satisfy

$$(k+3)\sin\Big((k+3)\cos^{-1}(\hat{y}_j^k)\Big)=(k+1)\sin\Big((k+1)\cos^{-1}(\hat{y}_j^k)\Big). \tag{3.12}$$

Set $\tilde{y}_0=\tilde{y}_1=-1, \tilde{y}_{N+1}=\tilde{y}_{N+2}=1$ and $\tilde{y}_{j+1}=\hat{y}_j^{N-1}$, $j=1,\ldots,N-1$, where $\{\hat{y}_j^{N-1}\}_{j=1}^{N-1}$ are the zero points of $P_{N-1}(y)$. Then, the set of points $\{\tilde{y}_j\}_{j=0}^{N+2}$, which we call the four-end-point collocation points, meets the requirement (ii).

In summary, we choose the collocation points in the following way:

Collocation points for (3.6)**:** The Chebyshev-Gauss-Lobatto and the four-end-point collocation points are used for x and y respectively.

Collocation points for (3.7)**:** The Chebyshev-Gauss-Lobatto collocation points are used for both x and y.

3.4. **Solution procedure of the fully discrete system.** The fully discrete system is obtained by evaluating the equations

$$\begin{aligned}\Big(\frac{4}{(\Delta t)^2}+\frac{2c}{\Delta t}\Big)w_{M,N}^{n+1}=F(w_{M,N}^{n+1},\mathbf{U}_{M,N}^{n})+\Big(\frac{3}{(\Delta t)^2}+\frac{c}{2\Delta t}\Big)w_{M,N}^{n+1}\\ +2\Big(\frac{1}{(\Delta t)^2}+\frac{c}{\Delta t}\Big)w_{M,N}^{n}-\Big(\frac{1}{(\Delta t)^2}+\frac{c}{2\Delta t}\Big)w_{M,N}^{n-1},\end{aligned} \tag{3.13}$$

$$\mathcal{L}(\mathbf{U}_{M,N}^{n+1})=\mathbf{f}(w_{M,N}^{n+1}) \tag{3.14}$$

on the collocation points given in the last subsection. To solve the nonlinear equations (3.13), we regard the solution $w_{M,N}^{n+1}$ as a fixed point of the following iterative scheme

$$\Big(\frac{4}{(\Delta t)^2}+\frac{2c}{\Delta t}\Big)w_{M,N}^{n+1,k+1}=F(w_{M,N}^{n+1,k},\mathbf{U}_{M,N}^{n})+\Big(\frac{3}{(\Delta t)^2}+\frac{c}{2\Delta t}\Big)w_{M,N}^{n+1,k}$$
$$+2\Big(\frac{1}{(\Delta t)^2}+\frac{c}{\Delta t}\Big)w_{M,N}^{n}-\Big(\frac{1}{(\Delta t)^2}+\frac{c}{2\Delta t}\Big)w_{M,N}^{n-1}. \quad (3.15)$$

To find the fixed point, we set $w_{M,N}^{n+1,0}=w_{M,N}^{n}$ as the initial guess, and compute $w_{M,N}^{n+1,k}$ iteratively for $k=1,2,\cdots$, until certain iterative error tolerance, say $\|w_{M,N}^{n+1,K}-w_{M,N}^{n+1,K-1}\|_\infty<\varepsilon$, is satisfied, then, $w_{M,N}^{n+1}\triangleq w_{M,N}^{n+1,K}$ is taken as the solution of the equation (3.13). Finally, substitute $w_{M,N}^{n+1}$ into the right hand side of the equation (3.14) to solve for $\mathbf{U}_{M,N}^{n+1}$.

4. Numerical experiments and results

In our numerical experiments, we set the Poisson ratio $\nu=0.3$, and choose $M=20$, $N=10$ for the spacial discretization, $L=100$ for the calculation of the mean and variance of the energy release rate (see (2.8) (2.9)), and $\varepsilon=10^{-10}$ for the fixed point iterative error tolerance, which turned out to be sufficient for convergence and reasonable accuracy. Special care should be taken to the values of the viscosity c and the time step Δt, since they have significant impact on the stability and efficiency of the algorithm. More precisely, if c is too big, the system will take a long time to converge to an equilibrium state, while if c is too small, it will have a very tight limit to the time step Δt to guarantee the stability of the dynamic process and the convergence of the fixed point iteration. Furthermore, the optimal values of c and Δt vary with the shape parameters and the normalized initial residual stress. In our numerical experiments, c varies in $[300,3000]$, and Δt varies in $[6\times10^{-6},10^{-5}]$.

4.1. Buckles' morphology and shape parameters.

Figure 5 shows typical numerical solutions of the discrete system (3.13)–(3.14) for various shape parameters (r_0,θ_0), where σ_0^*/σ_c^* is fixed at 20. As a comparison, the solution of the pinned circle model [13] is also shown in the figure in dashed lines. It is clearly seen that both of the parameters make non-negligible contributions to

the morphology of the buckle, especially, for some improper shape parameters, w may admit non-physical negative value.

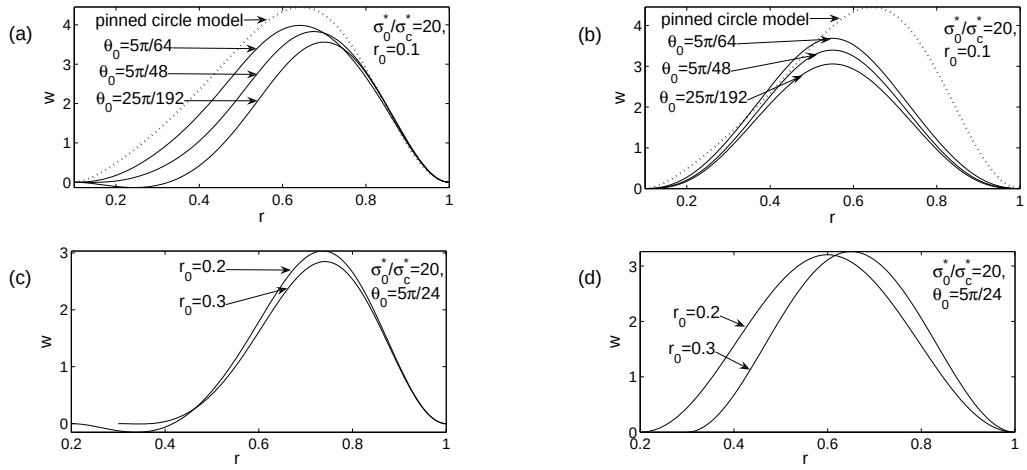

FIGURE 5: The normalized out-of-plane displacement w on the middle line ($\theta = 0$, (a), (c)) and the connection lines ($\theta = \theta_0$, (b), (d)).

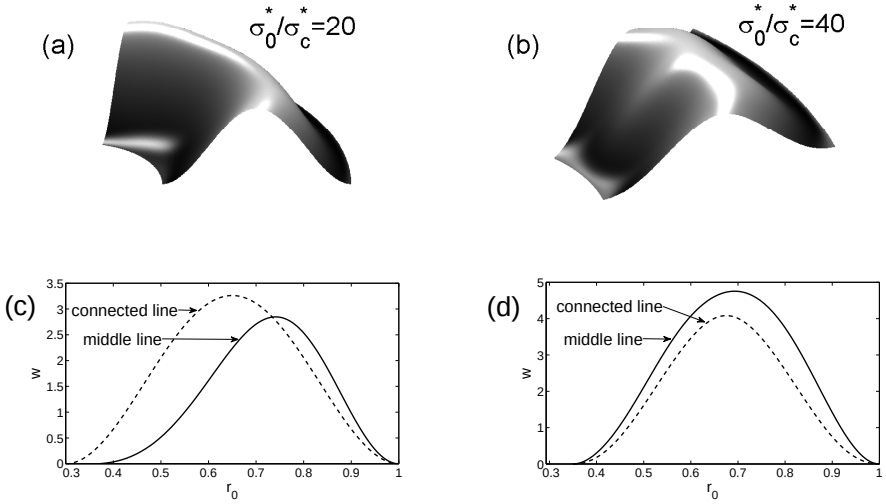

FIGURE 6: The morphology ((a), (b)) and normalized out-of-plane displacement ((c), (d)).

Figure 6 shows the typical morphologies of the numerical solutions for $\sigma_0^*/\sigma_c^* = 20$ and 40, which demonstrates that the initial residual stress has

a significant impact on the morphology of the telephone cord buckles. Our numerical experiments show that there is no telephone cord buckle solution when $\sigma_0^*/\sigma_c^* < 3.1$. Numerical experiments also show that, the morphology of deformation switches at about $\sigma_0^*/\sigma_c^* = 23$ from a one-hump-buckle (Figure 6(a)) to a two-hump-buckle (Figure 6(b)), and the maximum point of the displacement switches from the connection line to the middle line at the same time. Numerical difficulties also appear around $\sigma_0^*/\sigma_c^* = 23$, the numerical evidences show that there is a bifurcation point nearby, and there exists an interval on which the two types of morphologies coexist, although one of them may have a slightly greater local minimum of the variance of the energy release rate.

Figure 7 shows the relative distribution of the energy release rate in terms of a re-scaling function $f(\xi)$, which is given by (see (2.8))

$$f(\xi) = \begin{cases} \dfrac{\mathcal{G}\big(r_0, (\xi+1)\theta_0\big)}{\mathrm{m}(r_0,\theta_0)} - 1, & -2 \le \xi \le 0, \\ \dfrac{\mathcal{G}(1, (\xi-1)\theta_0)}{\mathrm{m}(r_0,\theta_0)} - 1, & 0 < \xi \le 2. \end{cases}$$

We see that the distribution of the energy release rate apparently depends on the shape parameter r_0 (Figure 7 (a)), and even more heavily on the shape parameter θ_0 (Figure 7 (b)), however, for a fixed σ_0^*/σ_c^* and for (r_0, θ_0) in a neighborhood of the minimizer $(\hat{r}_0, \hat{\theta}_0)$ (see (2.10)), the energy release rates on both the inner and outer arcs of the annular sector are reasonably close to the mean value $\mathrm{m}(r_0, \theta_0)$, especially away from the connection lines (Figure 7 (c)).

Our numerical experiments show that the variance $S(r_0, \theta_0)$ of the energy release rate behaves well in a neighborhood of the minimizer $(\hat{r}_0, \hat{\theta}_0)$ (see (2.10)). Figure 8 shows typical numerical results for $\sigma_0^*/\sigma_c^* = 15$, where the sub-figures (a) and (b) correspond to $\theta_0 = 41\pi/192$ and $r_0 = 0.23$ respectively. It is worth pointing out here that, for fixed σ_0, the minimizer $\hat{\hat{r}}_0(\theta_0)$ is not sensitive to θ_0.

Figure 9 shows, as functions of the normalized initial stress σ_0, the minimizer $(\hat{r}_0, \hat{\theta}_0)$ of the variance $S(r_0, \theta_0)$, and the width of the corresponding telephone cord buckles $T_w^* = (2 - (1 + \hat{r}_0)\cos(\hat{\theta}_0))R \triangleq T_w(\bar{E}h^{*5}/(384\pi^4\Gamma^*))^{1/4}$ (see (2.11)), where the jumps again suggest that there exist multiple solutions and bifurcation points.

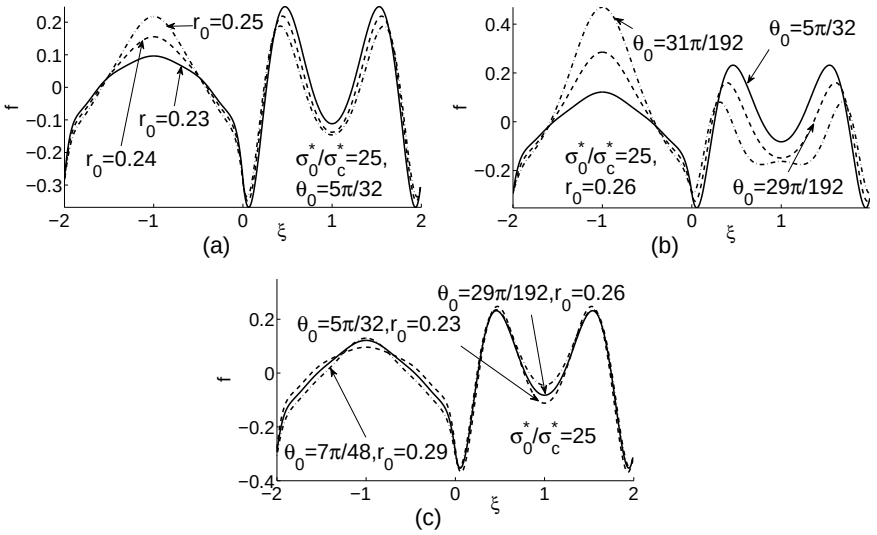

FIGURE 7: The relative distribution of the energy release rate with respect to $\sigma_0^*/\sigma_c^* = 25$.

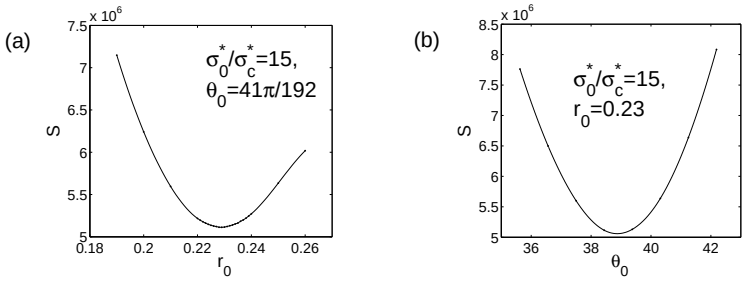

FIGURE 8: $S(r_0, \theta_0)$ as a function of r_0 and θ_0 with $\sigma_0^*/\sigma_c^* = 15$.

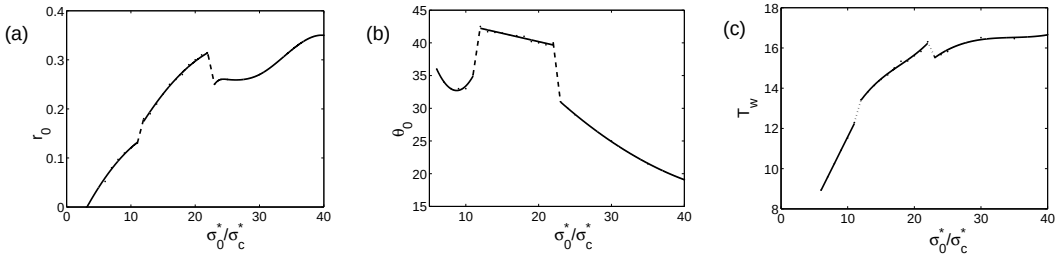

FIGURE 9: The minimizer $(r_0(\sigma_0^*/\sigma_c^*), \theta_0(\sigma_0^*/\sigma_c^*))$ of $S(r_0, \theta_0)$ ((a) and (b)) and the normalized width of the corresponding telephone cord buckles (c).

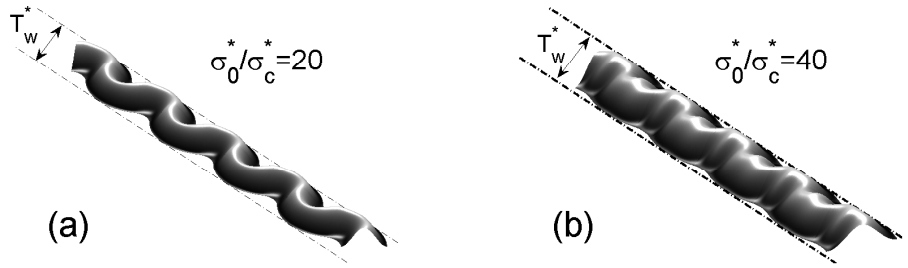

FIGURE 10: Typical numerical solutions of telephone cord buckles.

Typical numerical morphologies of the telephone-cord buckles produced by the annular sector model for $\sigma_0^*/\sigma_c^* = 20$ and 40 are shown in Figure 10.

4.2. **Comparison with the straight-sided buckles.** For simplicity and clarity, assuming that the Dundurs' parameter $\alpha = 0$ and thus in (2.7) $\omega = 52.1°$, we are going to compare the energy release rates and the phase angles of the straight-sided buckles with width $2b = R$ and the telephone cord buckles corresponding to the optimal shape parameter r_0 and the scale parameter R.

The numerical results of the energy release rates and the phase angles of the straight-sided [19] and telephone cord buckles are compared in Figure 11(a), (b), where the corresponding mean values are used for comparison. It is clearly seen that, for σ_0 small ($1 < \sigma_0^*/\sigma_c^* < 10$) the straight-sided buckles are energetically favorable, while for σ_0^*/σ_c^* large ($\sigma_0^*/\sigma_c^* > 10$) the telephone cord buckles are energetically favorable. The distributions of the phase angles of the numerical solutions with respect to certain typical initial stresses on the inner and outer arcs of the annular sectors are shown in Figure 11(c), where the phase angle is shown as a function of ξ as follows

$$\psi(\xi) = \begin{cases} \psi\big(r_0, (\xi+1)\theta_0\big), & -2 \le \xi \le 0, \\ \psi\big(1, (\xi-1)\theta_0\big), & 0 < \xi \le 2. \end{cases}$$

We see that the phase angle on the outer arc lies basically in $(-90°, -60°)$, and approaching $-90°$ as σ_0^*/σ_c^* increases, which indicates that the fracture front there is of mode II dominant, while on the inner arc it lies in $(-135°, -90°)$, and

thus will be treated as identical to $-90°$ to match the fracture theory (see [16]), which implies that the fracture front there is of pure mode Ⅱ. This asymmetry in the phase angle and thus in the fracture mode might be further explored to explain why the fracture fronts should grow on the two ends of the telephone cord buckles and in a zigzagged way. We notice also that, across $\sigma_0^*/\sigma_c^* = 23$, there is a jump in the average of the energy release rate and the average phase angle (Figure 11 (a), (b)), which suggests that there is a bifurcation point.

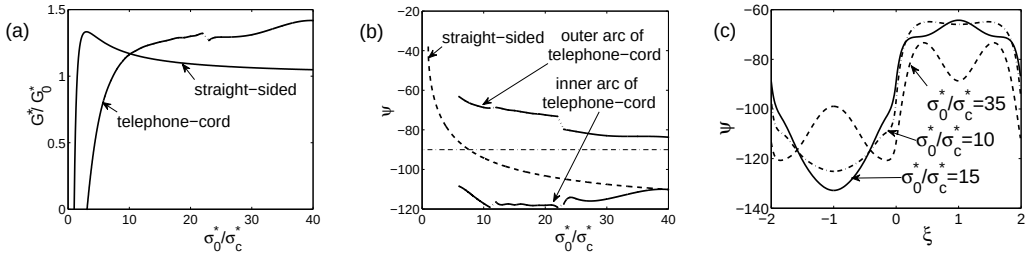

FIGURE 11: Comparison of the average energy release rates (a) and phase angles (b). The phase angle distributions of typical numerical solutions (c).

5. Comparison with experimental results

First, we compare our numerical results with a telephone cord buckle in a DLC film reported in [15] (see figures 2 and 3 there), where the film's thickness $h^* = 0.13\mu$m and the normalized maximum out-of-plane displacement on the middle line $w^m_{max} \doteq 4.1$. Noticing that w^m_{max} is a monotonously increasing function of σ_0^*/σ_c^*, we find that the corresponding $\sigma_0^*/\sigma_c^* \doteq 25$. With these data, the optimal shape parameters produced by our scheme are $r_0 = 0.26$ and $\theta_0 = 27°$, thus the central angle of the corresponding annular sector is $2\theta_0 = 54°$. We notice that the measure of the central angle is sensitive to the choice of the origin, in fact, if the origin of the angle is moved to the center of the inner arc of the annular sector, the central angle given by our numerical result will increase to $88°$. Thus our numerical results are in very good agreement with the physical experiment which produces the central angle of something around $75°$ (see figure 2 in [15]), considering that, when the angle is measured in physical experiments, the origin is set relatively closer to the center of the inner arc of the annular sector.

Next, we compare our numerical results with the physical experiments on telephone cord buckles in a DLC film reported in [13].

One of the important physical observations is that the width of the buckle seems to be an increasing function of the normalized initial residual stress σ_0. Such a relation is well reflected in Figure 9 (c), except that there is a twist near $\sigma_0^*/\sigma_c^* = 23$, where multiple solutions exist.

Our numerical results are also consistent with the physical observations that, for sufficiently large σ_0, there are two humps instead of one formed along the ridge of the buckle in each annular sector (see Figure 6 and compare it with figure 2 in [13]), and the central angle appears to be a decreasing function of σ_0 (see Figure 9 (b) for $\sigma_0^*/\sigma_c^* \geq 12$).

A key physical quantity measured in [13] is $\sigma_0^*/\hat{\sigma}_c^* = 6.5$, which separates the straight-sided and telephone-cord buckles observed in experiments. Notice that here $\hat{\sigma}_c^* = \bar{E}(\pi h^*)^2/(3(2b^*)^2)$ is the critical bifurcation stress of the straight-sided buckle with the width measured as $2b^* = R^*(1-r_0^*)$ (see figure 10 in [13]), where R^*, r_0^* stand for the scale and shape parameters of the critical telephone-cord buckle. While in our numerical result, the separation point is $\sigma_0^*/\sigma_c^* = 10$ (see Figure 11(a)), where σ_c^* is the critical bifurcation stress of the straight-sided buckle with the width measured as $2b = R^*$, and the corresponding shape parameter $r_0^* = 0.12$ (see Figure 9(a)), thus, we have $\sigma_0^*/\hat{\sigma}_c^* = (1-r_0)^2\sigma_0^*/\sigma_c^* = 7.7$. This again well matches the physical experiments.

6. Summary

The annular sector model, established in this paper for the telephone cord buckles of elastic thin films on rigid substrates, is based on the morphology assumptions that the delaminated region of the zigzagged part of the thin film can be divided into identical annular sectors and the elastic deformation is globally smooth and locally axis-symmetric with respect to the geometric central line of each annular sector (see Section 2.1), and on the discrete version of the Griffith criterion principle which states that the energy release rate on the arced fracture fronts has the minimum variance and at the same time its mean value equals to the toughness of the film-substrate interface (see Section 2.3).

A quasi-dynamic numerical method, combining the Newmark-β scheme and the Chebyshev collocation method, is designed to solve the governing von

Kárman plate equations expressed in polar coordinates. Comparisons of the numerical results with certain physical experiments well justified the model, and at the same time also raise interesting issues, such as to locate the bifurcation points and the coexistence intervals of multiple solutions corresponding to different types of telephone cord buckles' morphologies, etc., which we believe deserve further investigations.

On the other hand, the numerical results suggest that a more sophisticated model with more parameters might necessarily be introduced, should one intend to bring down the relative fluctuation of the energy release rate on the inner and outer arcs from the current level of around 20% (away from the connection lines, see Figure 5), so that the Griffith criterion could be better satisfied.

Acknowledgments

The research was supported by the Major State Basic Research Projects (2005CB321701), NSFC projects 10871011 and RFDP of China.

References

[1] A. G. Evans, D. R. Mumm, J. W. Hutchinson, G. H. Meier, F. S. Pettic, 2001, Mechanisms controlling the durability of thermal barrier coatings, Progress in Materials Science 46, 505-553.

[2] Y. Fu, H. Du, W. Huang, S. Zhang, M. Hu, 2004, TiNi-based thin films in MEMS applications: a review, Sensors and Actuators A: Physical 112, 395-408.

[3] P. J. Grundy, 1998, Thin film magnetic recording media, Journal of Physics-London-d Applied Physics 31, 2975.

[4] G. R. Irwin, 1960, Fracture mechanics, Stuctural Mechanics, edited by J. N. Goodier and N. J. Hoff, Pergamon Press, Oxford, 557-594.

[5] J. R. Rice, 1968, Mathematical analysis in the mechanics of fracture, Fracture, Vol. Ⅱ, edited by H. Liebowitz, Academic Press, New York, 191-311.

[6] J. Dundurs, 1969, Edge-bonded dissimilar orthogonal elastic wedges, Journal of Applied Mechanic 36, 650-652.

[7] A. S. Argon, V. Gupta, H. S. Landis, J.A. Cornie, 1989, Intrinsic toughness of interfaces between SiC coatings and substrates of Si or C fibre, Journal of Materials Science, 1207-1218.

[8] V. Sergo, and D. R. Clarke, 1998, Observation of subcritical spall propagation of a thermal barrier coating, Journal of the American Ceramic Society 81, 3237-3242.

[9] M. D. Thouless, 1993, Combined buckling and cracking of films, Journal of the American Ceramic Society 76, 2936-2938.

[10] N. Matuda, S. Bada, A. Kinbara, 1981, Internal stress, Young's modulus and adhesion energy of carbon films on glass substrates, Thin Solid Films, 81, 301-305.

[11] G. Gill, B. Rau, 1984, Buckling instability and adhesion of carbon layers. Thin Solid Films, 120, 109-121.

[12] J. Colin, F. Cleymand, C. Coupean, J. Grilhe, 2000, Worm-like delamination patterns of thin stainless steel films on polycarbonate substrates. Philos. Mag. A 80 (11), 2559-2568.

[13] M. Moon, K. Lee, K. Oh, J. Hutchinson, 2004, Buckle delamination on patterned substrates, Acta Materialia, 52, 3151-3159.

[14] M. Cordill, D. Bahr, N. Moody, W. Gerberich, 2007, Adhesion measurements using telephone cord buckles, Materials Science and Engineering: A Volume 443, 150-155.

[15] M. W. Moon, H. M. Jensen, J. W. Hutchinson, K. H. Oh, A. G. Evans, 2002, The characterization of tepephone cord buckling of compressed thin films on substrates, Journal of the Mechanics and Physics of Solids 50, 2355-2377.

[16] J. W. Hutchinson, and Z. Suo, 1992, Mixed mode cracking in layered materials, Advances in Applied Mechanics 29, 63-191

[17] H. M. Jensen, I. Sheinman, 2002, Numerical analysis of buckling-driven delamination, Int. J. Solids Struct 39, 3373-86.

[18] H. M. Jensen, M. D. Thouless, 1995, Buckling instability of straight edge cracks, Journal of Applied Mechanics 62, 620-625.

[19] H. M. Jensen, 1993, Effects of residual stresses in the blister test, International Journal of Solids and Structures 30, 779-795.

[20] H. M. Jensen, I. Sheinman, 2001, Straight-sided, buckling-driven delamination of thin films at high stress levels, International Journal of Fracture 110, 371-385.

[21] J. W. Hutchinson, M. Y. He, A. G Evans, 2000, The influence of imperfections on the nucleation and propagation of buckling driven delaminations,

Journal of the Mechanics and Physics of Solids 48, 709-734.

[22] G. Gioia, M. Ortiz, 1997, Delamination of compressed thin films, Advances in Applied Mechanics, 33, 119-192.

[23] D. Nir, 1984, Stress relief forms of diamond-like carbon thin films under internal compressive stress, Thin Solid Films, 112, 41-50.

[24] H. Jensen, J. Hutchinson, K. Kim, 1990, Decohesion of a cut prestressed film on a substrate. International Journal of Solids and Structures, 26, 1099-1114.

[25] J. Rice, 1988, Elastic fracture mechanics concepts for interfacial cracks. Journal of Applied Mechanics, 55, 98-103.

[26] Z. Suo, J. Hutchinson, 1990, Interface crack between two elastic layers, International Journal of Fracture, 43, 1-18.

[27] Z. Yosibash, R. M. Kirby, D. Gottlieb, 2004, Collocation methods for the solution of von-Karman dynamic non-linear plate systems, Journal of Computational Physics 200, 432-461.

[28] J. L. Humar, Dynamics of Stuctures, A. A. Balkema Publishers, 2002.

[29] R. M. Kirby and Z. Yosibash, 2004, Solution of von-Karman dynamic non-linear plate equations using a pseudo-spectral method, Computer Methods in Applied Mechanics and Engineering 193, 575-599.

[30] J. Shen, T. Tang, 2006, Spectral and high-order methods with applications, Science press, Beijing.

E-mail address: shasti0@pku.edu.cn, lizp@math.pku.edu.cn